Electric field-induced suppression of orbital-resolved electronic thermal conductivity in monolayer honeycomb borophene oxide (h-B_2O)

Farid Mohammadi,[a] Kavoos Mirabbaszadeh,*[a] and Houshyar Noshad,[a]

[a] Department of Physics and Energy Engineering, Amirkabir University of Technology (Tehran Polytechnic), P.O. Box: 159163-4311, Tehran, Iran.

1 Tight Binding Hamiltonian

In this section, our theoretical calculations commence with the evaluation of a h-B_2O tight-binding (TB) Hamiltonian. Within the realm of condensed matter physics, the reciprocal-space Hamiltonian formulation is crucially influenced by two key factors: The first factor pertains to the geometric structure in real space, while the second factor relates to the atomic orbitals. These factors collectively contribute to the comprehensive description of the electronic properties under investigation. Consequently, we begin our analysis by examining the geometric configuration of h-B_2O, where it is evident that the monolayer exhibits a fully planar structure, comprising honeycomb lattices that are stretched along the x-axis. The h-B_2O monolayer demonstrates crystallization in the orthorhombic lattice, characterized by the space group Cmmm (No. 65), furthermore, this structure demonstrates a C_{2v} symmetry. unit cell, is composed of two B and one O atoms (1a). The First Brillouin Zone (FBZ) associated with the structure is represented as a distorted hexagonal shape (due to $\pi/2$ rotation of the unit cell) (1b). The optimum values for the lattice constants, α and β, are 2.806 Å and 7.127 Å, respectively. The lengths of the equilibrium bonds B-B and B-O are 1.706 Å and 1.341 Å, respectively. Due to the presence of the oxygen atom, we have a deformed hexagonal structure whose bond angles are 107.8° and 126.1° respectively [1]. It is time to elucidate the atomic orbitals of h-B_2O. By considering the atomic numbers of boron ($1s^2 2s^2 2p^1$) and oxygen ($1s^2 2s^2 2p^4$), it can be determined that h-B_2O exhibits four orbitals, namely s, p_x, p_y, and p_z. These orbitals determine the electronic properties of h-B_2O. Within this particular framework, we direct our attention toward the orbitals whose energy bands are close proximity to the Fermi level, as they assume a pivotal function in determining the electronic characteristics. Hence, our specific emphasis is directed toward two orbitals, namely P_y, and P_z [2**?**]. But, when considering graphene and β_{12}-borophene, it is observed that the P_z orbitals play a prominent role in the conduction process, resulting in the Hamiltonian being exclusively formulated based on these orbitals[3, 4].

Following the elucidation provided regarding the geometric arrangement and the influential orbitals in the electronic characteristics, a TB model is employed to accurately depict the low-energy band structure of h-B_2O. Despite the presence of two B atoms and one O atom in the primitive cell, it is possible to simplify the model by removing the O sites. Since the oxygen atoms occupy a bridging position within the structure, This simplification does not compromise

*Email: mirabbas@aut.ac.ir

the symmetry of the model [2**?**]. Therefore, to construct a final version of the TB model, we shall take into account the contributions of the P_y and P_z orbitals that are associated with B atoms within the unit cell (see Fig. 2). In order to derive the TB Hamiltonian in the second quantization representation, we analyze each orbital individually. let us begin by examining the P_z orbitals.

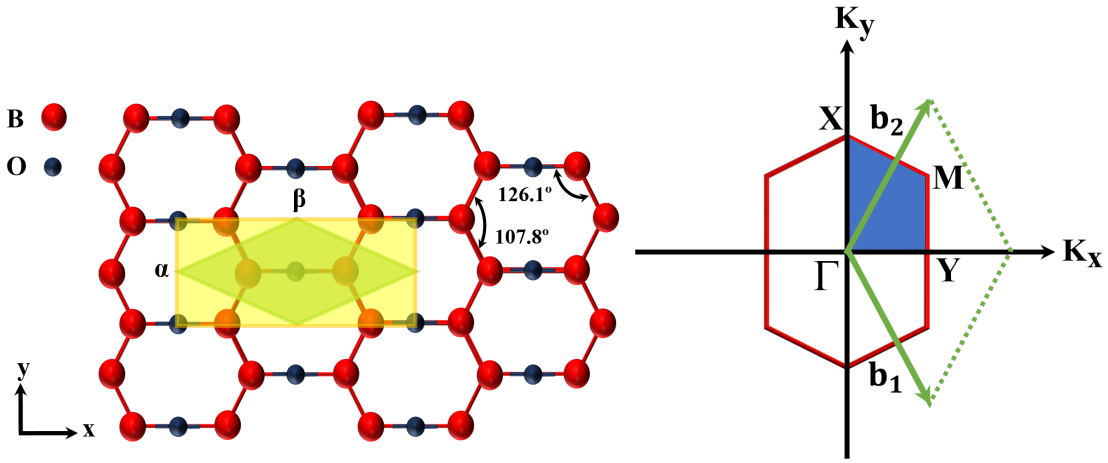

(a) (b)

Figure 1: (a) The crystal structure of h-B2O, with the unit cell indicated by the green rhombus and lattice constants labeled as α and β. (b) First Brillouin Zone (FBZ) of h-B2O in reciprocal space, including high-symmetry points.

Initially, in relation to the designated atoms within the h-B_2O structure, we shall allocate distinct positions to facilitate the identification of atom hoppings i.e.

$$a \Rightarrow i, \qquad b \Rightarrow j$$

To facilitate comprehension, we initially partition the Hamiltonian into two distinct components:

$$\mathscr{H}_{p_z}^{\vec{k}} = \underbrace{\mathscr{H}_0}_{\text{On-site energies}} + \underbrace{\mathscr{H}_1}_{\text{Hopping energies}} \tag{1}$$

the first section calculates on-site energies, while the second part displays the different hoppings to the nearest-neighbors $\langle NN \rangle$. So,

$$\mathscr{H}_0 = \underbrace{\sum_i \varepsilon_a a_i^\dagger a_i}_{\text{a atom}} + \underbrace{\sum_j \varepsilon_b b_j^\dagger b_j}_{\text{b atom}} \tag{2}$$

$$\mathscr{H}_1 = \underbrace{\sum_{<ij>} t_{ab} a_i^\dagger b_j}_{b \longmapsto a} + \underbrace{\sum_{<ij>} t_{ba} b_j^\dagger a_i}_{a \longmapsto b} \tag{3}$$

Two on-site energies for various atoms in the unit cell (ε_a and ε_b) are contained in $\mathscr{H}_0$, and the hoppings from the a atom to the nearest b atoms and vice versa are displayed in $\mathscr{H}_1$. The creation and annihilation operators are denoted as $\{a_i, b_i\}$ and $\{a_i^\dagger, b_i^\dagger\}$, respectively. The final matrix form will be as follows:

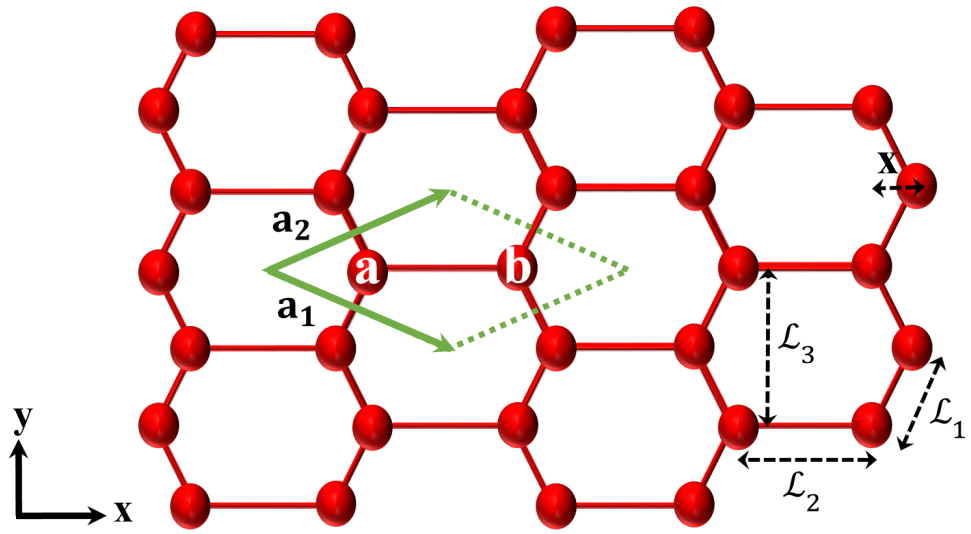

(a)

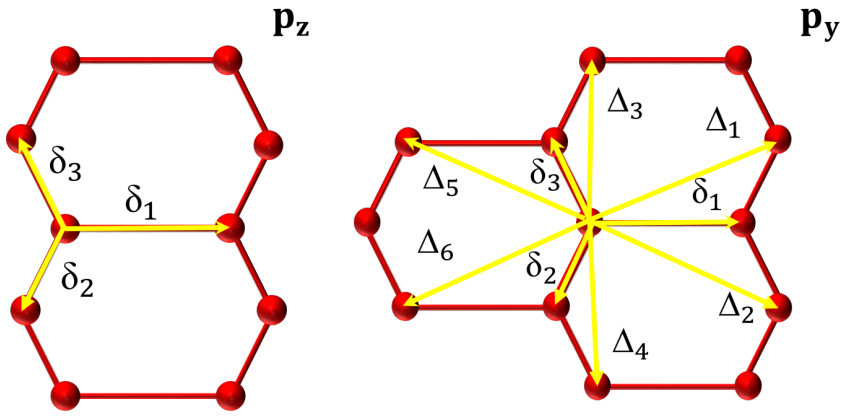

(b)

Figure 2: (a) Crystal structure of h-B_2O without oxygen atoms, showing two motif atoms, labeled a and b, in the unit cell. (b) P_y and P_z orbitals of the boron atoms and their respective neighboring atoms.

$$\mathscr{H}_{p_z}^{\vec{k}} = \begin{bmatrix} \varepsilon_a a_i^\dagger a_i & t_{ij} a_i^\dagger b_j \\ t_{ji} b_j^\dagger a_i & \varepsilon_b b_j^\dagger b_j \end{bmatrix} \tag{4}$$

The coefficient ε_a and ε_b represents the on-site energy of electrons.Since the atoms are the same, ε_a=ε_b. Now, the calculation of creation and annihilation operators is necessary. The relationship between these operators in both real space and reciprocal space can be described as follows:

$$
\begin{aligned}
a_i &= \frac{1}{\sqrt{N}} \sum_k a_k e^{i\vec{k}.\vec{R}_i} \\
a_i^\dagger &= \frac{1}{\sqrt{N}} \sum_k a_k^\dagger e^{-i\vec{k}.\vec{R}_i} \\
b_j &= \frac{1}{\sqrt{N}} \sum_k b_k e^{i\vec{k}.\vec{R}_j} \\
b_j^\dagger &= \frac{1}{\sqrt{N}} \sum_k b_k^\dagger e^{-i\vec{k}.\vec{R}_j}
\end{aligned} \tag{5}
$$

where N is the number of unit cells in our system. Hence, we use 5 to calculate $a_i^\dagger b_j$:

$$
\begin{aligned}
\sum_{\langle i,j \rangle} a_i^\dagger b_j &= \left[\frac{1}{\sqrt{N}} \sum_k a_k^\dagger e^{-i\vec{k}.\vec{R}_i} \right] . \left[\frac{1}{\sqrt{N}} \sum_{k'} b_{k'} e^{i\vec{k'}.\vec{R}_j} \right] \\
&= \sum_{\langle i,j \rangle} \sum_k \sum_{k'} \frac{1}{N} (e^{-i\vec{k}.\vec{R}_i} . e^{i\vec{k'}.\vec{R}_j}) a_k^\dagger b_{k'}
\end{aligned} \tag{6}
$$

By multiplying $e^{i\vec{k'}.\vec{R}_i} . e^{-i\vec{k'}.\vec{R}_i}$ in 6, we will obtain:

$$
\begin{aligned}
\sum_{\langle i,j \rangle} a_i^\dagger b_j &= \sum_{\langle i,j \rangle} \sum_k \sum_{k'} \frac{1}{N} (e^{-i\vec{k}.\vec{R}_i} . e^{i\vec{k'}.\vec{R}_i})(e^{-i\vec{k}.\vec{R}_i} . e^{i\vec{k'}.\vec{R}_j}) a_k^\dagger b_{k'} \\
&= \sum_k \left[\frac{1}{N} \sum_{k'} e^{i(\vec{k'}-\vec{k}).\vec{R}_i} \right] . \left[\sum_{\langle i,j \rangle} e^{i(\vec{R}_j - \vec{R}_i).\vec{k'}} \right] a_k^\dagger b_{k'} \\
&= \sum_k \sum_{\vec{\delta}_{NN}} e^{i(\vec{\delta}_{NN}.\vec{k})} a_k^\dagger b_k = \sum_k f_{\vec{k}} a_k^\dagger b_k
\end{aligned} \tag{7}
$$

where $\vec{\delta}_{NN} = \vec{R}_j - \vec{R}_i$ is lattice vector and

$$
f_{\vec{k}} = \sum_{\vec{\delta}_{NN}} e^{i(\vec{k}.\vec{\delta}_{NN})}
$$

In a similar vein, upon substituting the values of variables $b_j^\dagger$ and a_i into the second component of 3 , we obtain:

$$
\begin{aligned}
\sum_{\langle i,j \rangle} a_i b_j^\dagger &= \sum_k \left[\frac{1}{N} \sum_{k'} e^{i(\vec{k'}-\vec{k}).\vec{R}_j} \right] . \left[\sum_{\langle i,j \rangle} e^{i(\vec{R}_i - \vec{R}_j).\vec{k'}} \right] b_k^\dagger a_{k'} \\
&= \sum_k \sum_{\vec{\delta}_{NN}} e^{-i(\vec{\delta}_{NN}.\vec{k})} b_k^\dagger a_k = \sum_k f_{\vec{k}}^* b_k^\dagger a_k
\end{aligned} \tag{8}
$$

where

$$
f_{\vec{k}}^* = \sum_{\vec{\delta}_{NN}} e^{-i(\vec{\delta}_{NN}.\vec{k})} \tag{9}
$$

It is now appropriate to present the coordinates of the $\langle NN \rangle$ (all units are in Å):

$$\mathcal{L}_1 = 1.706 = \underbrace{(B - B)}_{\text{bond length}}$$

$$\mathcal{L}_2 = 2.682 = 2\underbrace{(B - O)}_{\text{bond length}}$$

$$x = \sqrt{\mathcal{L}_1^2 - (\mathcal{L}_3/2)^2} = 0.970$$

$$\vec{a}_1 = (\alpha, -\mathcal{L}_3/2) = (3.652, -1.403)$$

$$\vec{a}_2 = (\alpha, \mathcal{L}_3/2) = (3.652, 1.403)$$

$\vec{a}_1$ and $\vec{a}_2$ are the constitutive vectors of the unit cell in real space. where $\alpha = x + \mathcal{L}_2$. Finally, for hopping a to b:

$$\begin{aligned} t_1 \rightarrow & \ \{\vec{\delta}_1 = (\mathcal{L}_2, 0) = (2.682, 0) \\ t_2 \rightarrow & \begin{cases} \vec{\delta}_2 = (-x, -\mathcal{L}_3/2) = (-0.970, -1.403) \\ \vec{\delta}_3 = (-x, +\mathcal{L}_3/2) = (-0.970, 1.403) \end{cases} \end{aligned} \tag{10}$$

and b to a:

$$\begin{aligned} \vec{\delta'}_1 &= (-\mathcal{L}_2, 0) = (-2.682, 0) \\ \vec{\delta'}_2 &= (x, -\mathcal{L}_3/2) = (0.970, -1.403) \\ \vec{\delta'}_3 &= (x, +\mathcal{L}_3/2) = (0.970, 1.403) \end{aligned} \tag{11}$$

Based on condition $a_i b_j = 2\pi\delta_{ij}$ (δ_{ij} is kronecker delta), it is possible to derive the constitutive vectors of the FBZ in the reciprocal lattice.

$$\begin{aligned} \vec{b}_1 &= \pi(1/\alpha, -2/\mathcal{L}_3) \\ \vec{b}_2 &= \pi(1/\alpha, 2/\mathcal{L}_3) \end{aligned} \tag{12}$$

Finally, the Hamiltonian for the p_z orbital will be as follows, and we will use it in current work to calculate the band structure (BS) and density of states (DOS), as well as to validate our results against density functional theory (DFT) calculations:

$$\mathscr{H}_{p_z}^{\vec{k}} = \begin{bmatrix} \varepsilon_a & f_{\vec{k}} \\ f_{\vec{k}}^* & \varepsilon_b \end{bmatrix} \tag{13}$$

where the $f_{\vec{k}}$ is defined as:

$$f_{\vec{k}} = t_1 e^{ik_x(\mathcal{L}_2)} + [t_2 e^{-ik_x(x)} \cos(k_y(\mathcal{L}_3/2))] \tag{14}$$

Now, we aim to compute the Hamiltonian for p_y orbitals using the same procedure. So,

$$\mathscr{H}_{p_y}^{\vec{k}} = \underbrace{\mathscr{H}_0}_{\text{On-site energies}} + \underbrace{\mathscr{H}_1}_{\text{Hopping energies}} \tag{15}$$

the first section relate to on-site energies of p_y orbitals, while the second part displays the different hoppings to the $\langle NN \rangle$ and next-nearest-neighbors ($\langle NNN \rangle$). As we mentioned, there is one important difference with the p_z orbitals that we must consider: the next-nearest-neighbor interactions for p_y orbitals. Because the p_y orbital lies in the plane of B_2O, considering interactions with $\langle NNN \rangle$ becomes indispensable and should not be disregarded. Therefore, for p_y orbitals, there are three $\langle NN \rangle$ ($\vec{\delta}_1$, $\vec{\delta}_2$, and $\vec{\delta}_3$), sharing the same coordinates as those obtained for the p_z orbitals. Additionally, there are six $\langle NNN \rangle$ ($\Delta_1, ..., \Delta_6$) (see Fig. **??**). resulting,

$$\begin{aligned}
t_1 \rightarrow & \ \{\vec{\delta}_1 = (\mathcal{L}_2, 0) \\
t_2 \rightarrow & \begin{cases} \vec{\delta}_2 = (-x, -\mathcal{L}_3/2) \\ \vec{\delta}_3 = (-x, +\mathcal{L}_3/2) \end{cases} \\
t_3 \rightarrow & \begin{cases} \vec{\Delta}_3 = (0, +\mathcal{L}_3) \\ \vec{\Delta}_4 = (0, -\mathcal{L}_3) \end{cases} \\
t_4 \rightarrow & \begin{cases} \vec{\Delta}_1 = (\alpha, +\mathcal{L}_3/2) \\ \vec{\Delta}_2 = (\alpha, -\mathcal{L}_3/2) \\ \vec{\Delta}_5 = (-\alpha, +\mathcal{L}_3/2) \\ \vec{\Delta}_6 = (-\alpha, -\mathcal{L}_3/2) \end{cases}
\end{aligned} \tag{16}$$

in graphene, which has a regular hexagonal structure with equal bond distances, all bonds share a common hopping parameter [5]. However, in h-B_2O, the presence of oxygen at the bridge site causes the hexagon to deform, resulting in different hopping parameters. Finally:

$$\mathscr{H}_{p_y}^{\vec{k}} = \begin{bmatrix} \varepsilon_a & g_{\vec{k}} \\ g_{\vec{k}}^* & \varepsilon_b \end{bmatrix} \tag{17}$$

where $g_{\vec{k}}$ is defined as:

$$\begin{aligned}
g_{\vec{k}} = & \ t_1 e^{ik_x(\mathcal{L}_2)} + [t_2 e^{-ik_x(x)} \cos(k_y(\mathcal{L}_3/2))] \\
& + 2t_3 \cos(\mathcal{L}_3 k_y) + 4t_4 \cos(k_y(\mathcal{L}_3/2)) \cos(\alpha k_x)
\end{aligned} \tag{18}$$

it is worth noting that, due to the orthogonality of the p_y and p_z orbitals, they are found to be independent and decoupled in the TB formalism.

2 The pristine band structure and density of states of h-B_2O

Here, we present the BS of the pristine h-B_2O monolayer corresponding to the P_y and P_z orbitals over a broader energy range than that shown in the main manuscript, in order to clearly reveal the on-site energies. The two Dirac cones are located at 4.12 eV for the P_y orbital and 3.11 eV for the P_z orbital (see the left panel of Fig. 3). In addition, the DOS diagram highlights not only these on-site energies but also several Van Hove singularities (VHSs), which correspond to the extrema points in the band structure (see the right panel of Fig. 3).

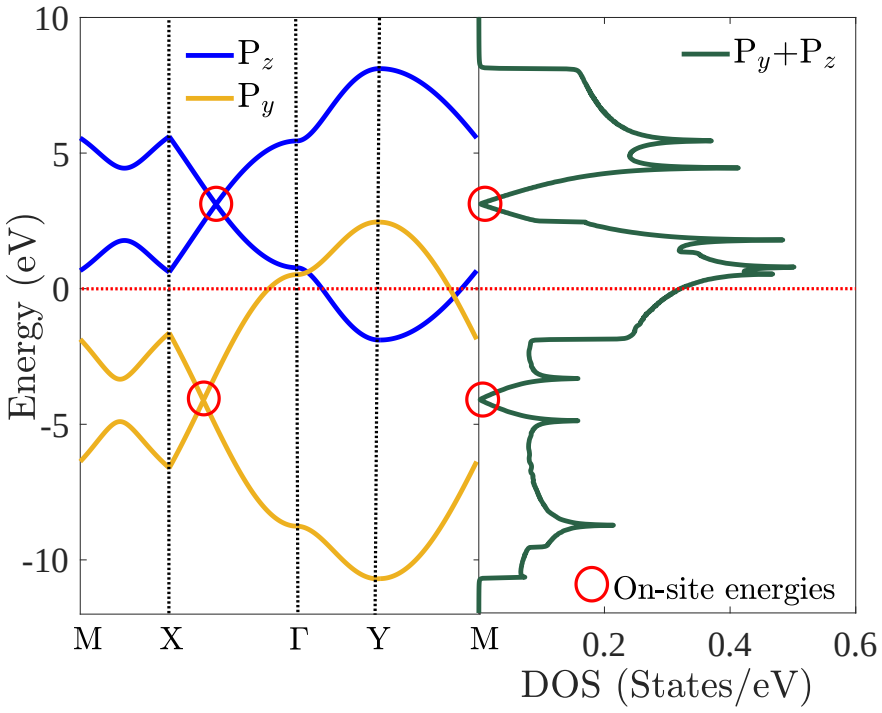

Figure 3: Band structure (left panel) and density of states (right panel) of monolayer h-B_2O .

3 group velocity analysis

The presented maps illustrate the distribution of the $|V_x|$ component associated with the P_z orbital in the first Brillouin zone. Figure 4a shows the dependence of $|V_x|$ on the magnitude of the wave vector $|k|$. The plot reveals a steep dispersion behavior near the band transition regions, where the velocity reaches approximately 7×10^5 m/s. Figure 4b presents the two–dimensional distribution of $|V_x|$ in the (k_x, k_y) plane. The highest velocity values are concentrated near the center of the Brillouin zone ($k_x = 0, k_y = 0$), while the velocities gradually decrease toward the zone boundaries. This behavior indicates a moderate anisotropy in the velocity distribution and is consistent with the quasi-zigzag structural characteristics of the h-B_2O lattice. The distribution of the $|V_x|$ component associated with the P_y orbital in the first Brillouin zone is displayed in Figures 4c and 4d. As shown in Figure 4c, $|V_x|$ exhibits a narrower variation with $|k|$, with maximum values around 5×10^5 m/s. The dispersion is less steep than that of the P_z orbital, indicating weaker band curvature and hence lower group velocities. Figure 4d displays the corresponding two–dimensional velocity map in the (k_x, k_y) plane. The highest $|V_x|$ values appear in an elongated region around the Brillouin-zone center, forming a more anisotropic pattern compared with the P_z orbital. The velocity magnitude gradually decreases toward the zone boundaries. Overall, these results show that the P_y orbital contributes less effectively to electronic transport along the x direction.

The presented maps illustrate the distribution of the $|V_y|$ component associated with the P_z orbital in the first Brillouin zone. Figure 5a shows the dependence of $|V_y|$ on the magnitude of the wave vector $|k|$. The results indicate a pronounced dispersion behavior, where the velocity increases rapidly with $|k|$ and reaches maximum values close to 1.1×10^6 m/s. This behavior reflects a strong band curvature along the y direction. Figure 5b presents the two–dimensional distribution of $|V_y|$ in the (k_x, k_y) plane. The highest velocity values are mainly concentrated near the central region of the Brillouin zone and extend predominantly along the k_y direction.

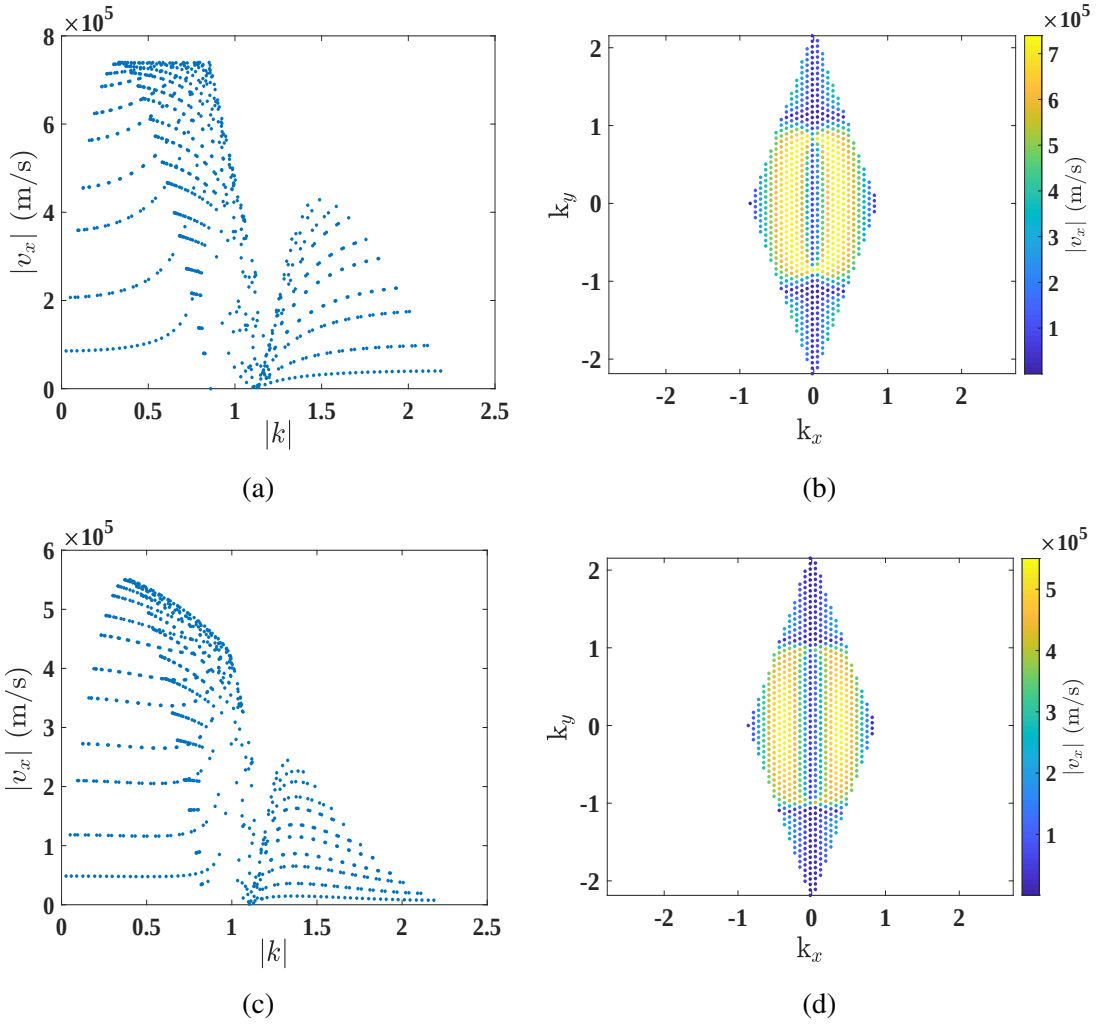

Figure 4: Electronic group velocities $|v_x|$ for the P_z (a,b) and P_y (c,d) orbitals within the first Brillouin zone.

This pattern reveals a noticeable anisotropy in the velocity distribution, suggesting that charge carriers can propagate more efficiently along the y direction for the P_z orbital. The distribution of the $|V_y|$ component associated with the P_y orbital in the first Brillouin zone is displayed in Figures 5c and 5d. As shown in Figure 5c, $|V_y|$ varies with $|k|$ within a narrower range compared with the P_z orbital, with maximum values of approximately 8×10^5 m/s. The dispersion slope is therefore smaller, indicating relatively weaker band curvature and lower group velocities. Figure 5d shows the corresponding two–dimensional velocity map in the (k_x, k_y) plane. The highest $|V_y|$ values are again located near the center of the Brillouin zone, forming a relatively localized and anisotropic distribution. The velocity magnitude gradually decreases toward the zone boundaries. Overall, the comparison between the P_z and P_y orbitals indicates that the P_z orbital contributes more strongly to carrier transport along the y direction due to its larger group velocities and stronger dispersion characteristics.

4 BS and DOS of h-B_2O under Perpendicular Electric Field

In this section, we present the BS and DOS of the P_y (see Fig. 6a) and P_z (see Fig. 6b) orbitals separately under a perpendicular electric field with potentials of {0, 0.5, 0.75, and 1 eV}. It

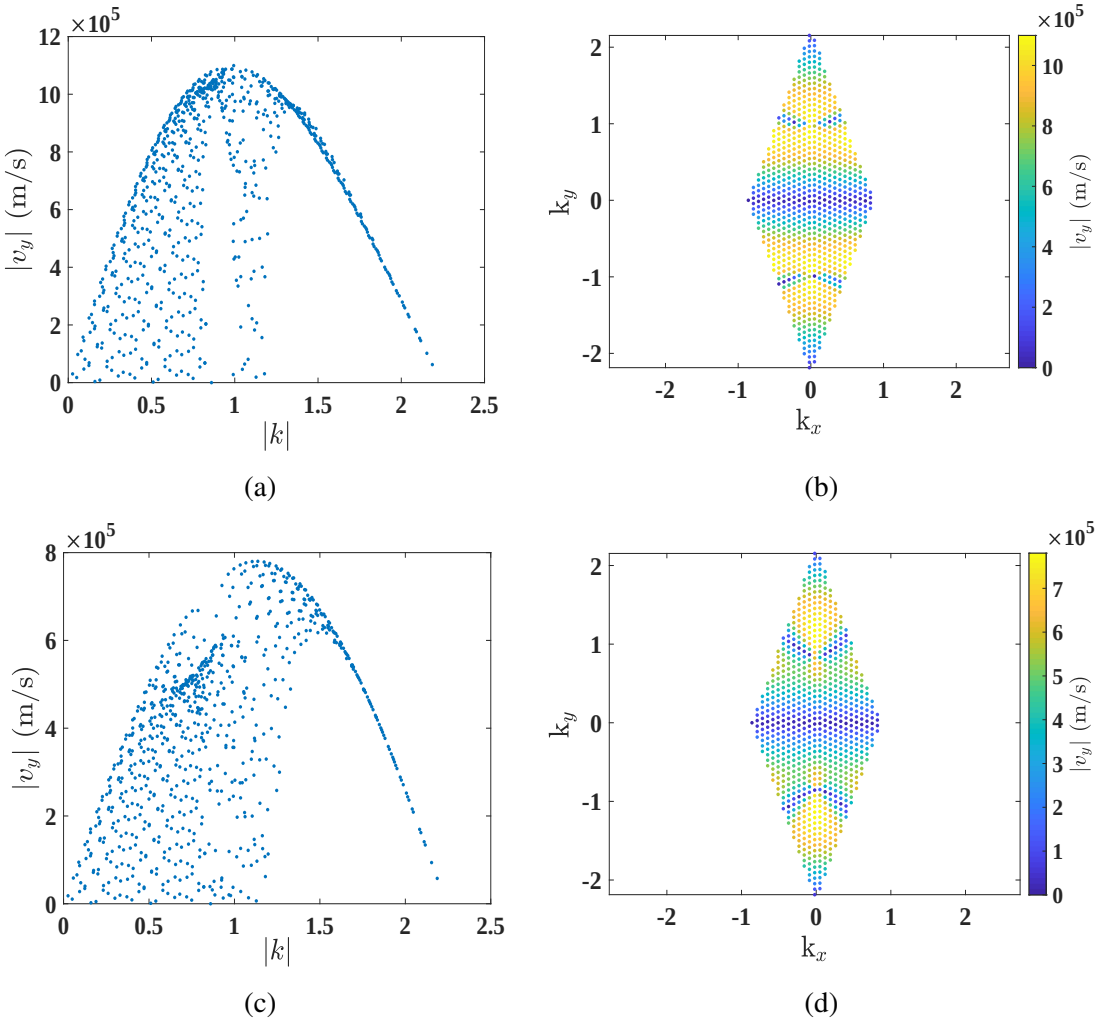

Figure 5: Electronic group velocities $|v_y|$ for the P_z (a,b) and P_y (c,d) orbitals within the first Brillouin zone.

is clearly observed that for both orbitals, only the second path (X to Γ) undergoes significant changes, where an energy gap opens following the relation $E_g = 2V$. In contrast, the other paths remain nearly unchanged compared to the pristine state.

Subsequently, we present the BS and DOS of h-B_2O under the influence of an electric field for both the ungated and 1 eV gated cases, across a broader energy range than that shown in the main manuscript. This reveals a clearer illustration of the opening of Dirac points, which are also evident in the DOS plots. Additionally, the DOS diagram clearly shows a shift in the position of the VHSs under the applied field 7.

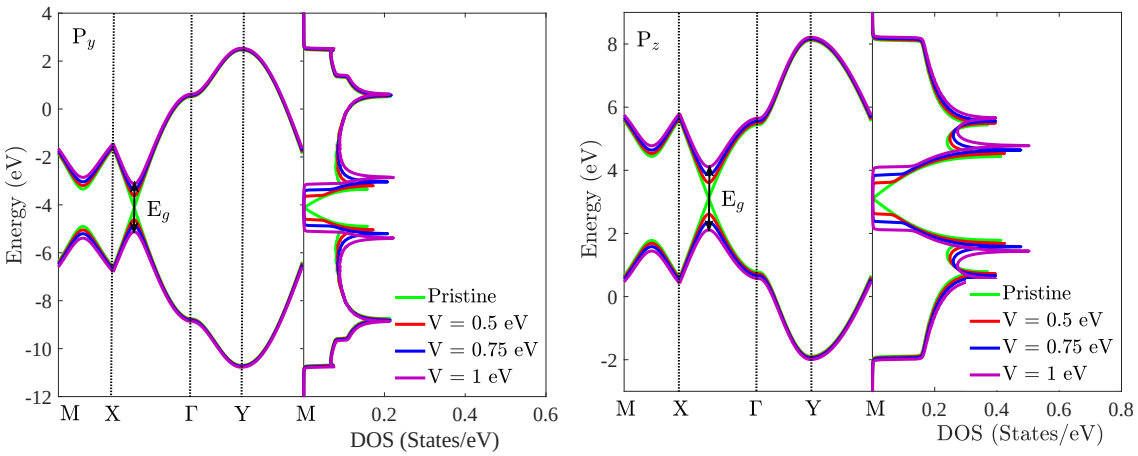

(a) (b)

Figure 6: (a) BS and DOS for the P_y orbital, and (b) P_z orbital at different potential values: {0, 0.5 eV, 0.75 eV, and 1 eV} .

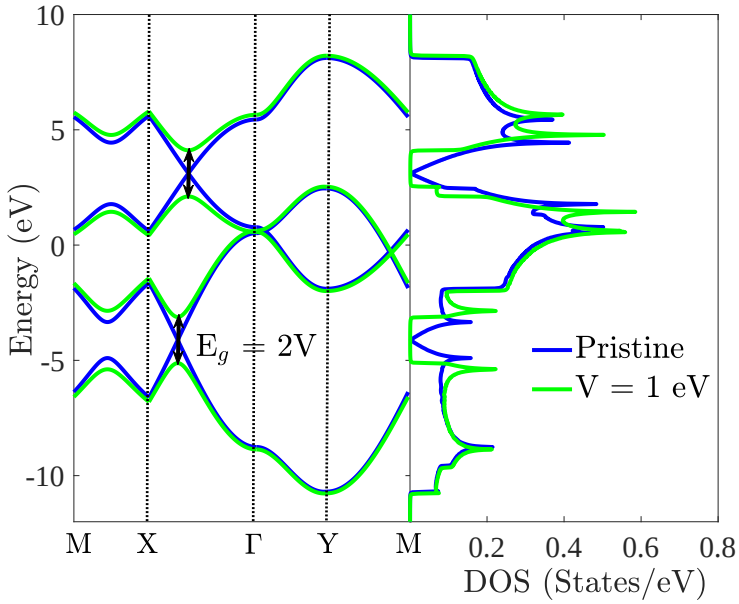

Figure 7: BS (left panel) and DOS (right panel) of monolayer h-B_2O for zero bias (V = 0) and a bias of V = 1 eV.

5 Orbital Electronic Thermal Conductivity under a Perpendicular Electric Field

We present the results of electronic thermal conductivity (ETC) for the P_y and P_z orbitals under different potential values, in the three directions: xx (8), yy (9), and xy (10). It is evident that the ETC of both the P_y and P_z orbitals decreases in all three directions as the applied potential increases.

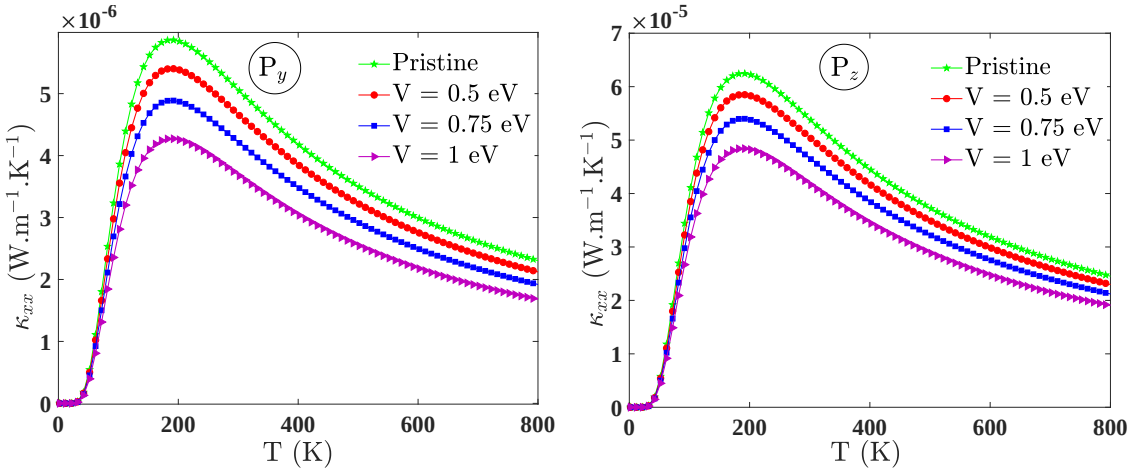

Figure 8: (a) κ_{xx} of the P_y orbital, and (b) P_z orbital of h-B_2O at different potential values: {0, 0.5 eV, 0.75 eV, and 1 eV}.

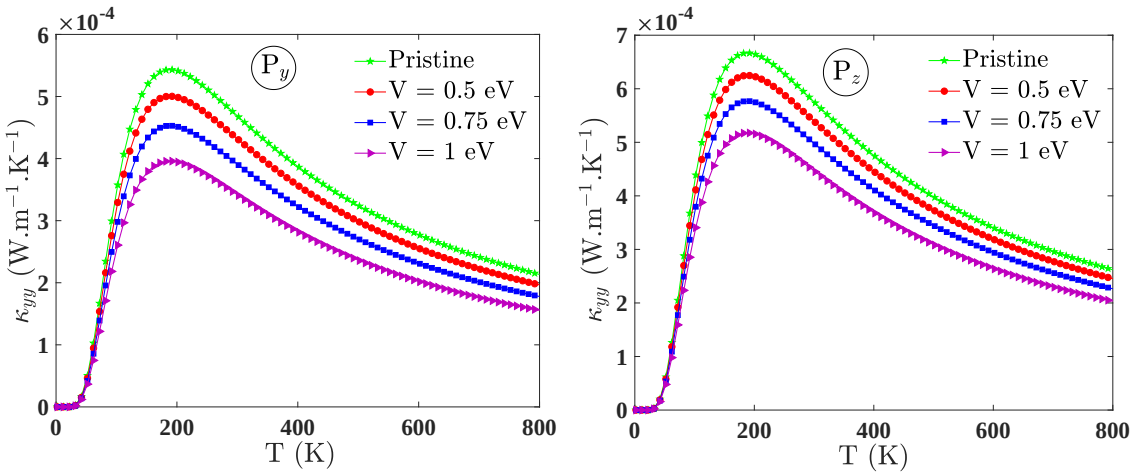

Figure 9: (a) κ_{yy} of the P_y orbital, and (b) P_z orbital of h-B_2O at different potential values: {0, 0.5 eV, 0.75 eV, and 1 eV}.

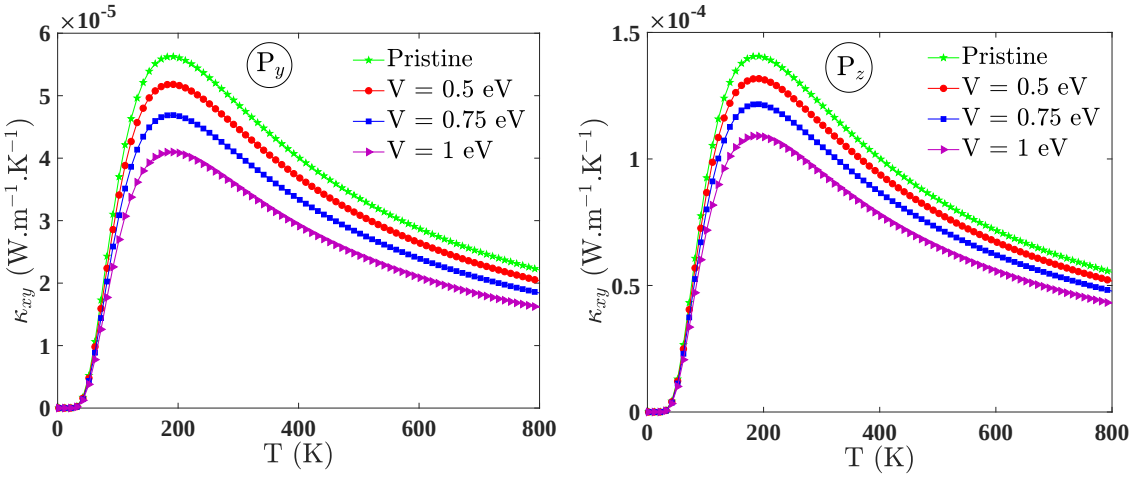

(a) (b)

Figure 10: (a) κ_{xy} of the P_y orbital, and (b) P_z orbital of h-B_2O at different potential values: {0, 0.5 eV, 0.75 eV, and 1 eV}.

Finally, we have plotted the ETC as a function of potential for these two orbitals at room temperature (11).

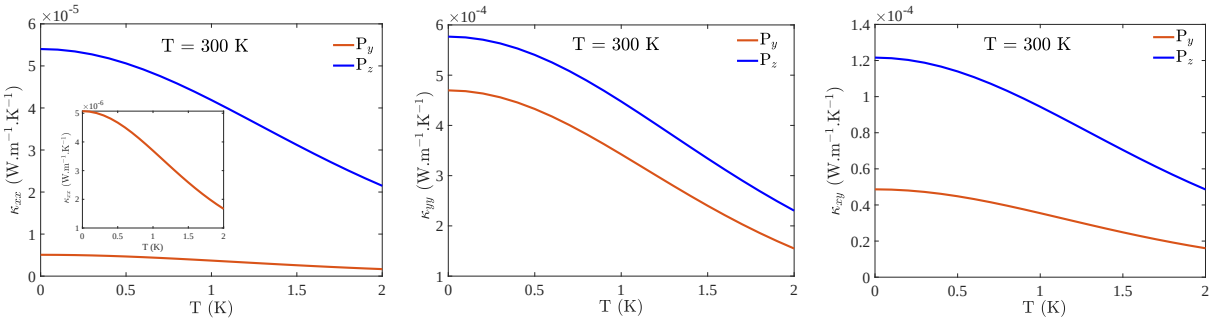

(a) (b) (c)

Figure 11: (a) κ_{xx}, (b) κ_{yy}, and (c) κ_{xy} of h-B_2O for P_y and P_z orbitals as a function of potential at room temperature (T = 300 K).

References

[1] Luo Yan, Peng-Fei Liu, Hengtao Li, Yong Tang, Junjie He, Xingyong Huang, Bao-Tian Wang, and Liujiang Zhou. Theoretical dissection of superconductivity in two-dimensional honeycomb borophene oxide b2o crystal with a high stability. *npj Computational Materials*, 6(1):94, 2020.

[2] Chengyong Zhong, Weikang Wu, Junjie He, Guangqian Ding, Yi Liu, Dengfeng Li, Shengyuan A Yang, and Gang Zhang. Two-dimensional honeycomb borophene oxide: strong anisotropy and nodal loop transformation. *Nanoscale*, 11(5):2468–2475, 2019.

[3] Jeil Jung and Allan H MacDonald. Tight-binding model for graphene π-bands from maximally localized wannier functions. *Physical Review BCondensed Matter and Materials Physics*, 87(19):195450, 2013.

[4] Motohiko Ezawa. Triplet fermions and dirac fermions in borophene. *Physical Review B*, 96(3):035425, 2017.

[5] Stephanie Reich, Janina Maultzsch, Christian Thomsen, and Pablo Ordejon. Tight-binding description of graphene. *Physical Review B*, 66(3):035412, 2002.